UNIVERSITY OF CALIFORNIA

Santa Barbara

Imaging Central Pacific Upper Mantle using P-wave Tomography and Receiver Functions

A Thesis submitted in partial satisfaction of the

requirements for the degree Master of Science in Earth Science

by

Lun Zhang

Committee in charge:

Professor Zachary Eilon, Chair

Professor Toshiro Tanimoto

Professor Chen ji

June 2021

The thesis of Lun Zhang is approved.

_____

Chen Ji

_____

Toshiro Tanimoto

_____

Zachary Eilon, Committee Chair

June 2021

Imaging Central Pacific Upper Mantle using P-wave Tomography and Receiver Functions

by

Lun Zhang

ACKNOWLEDGEMENTS

I would like to express my special thanks of gratitude to my research advisor Prof. Zachary Eilon, who helped me a lot in outlining my research blueprint, solving various difficulties and improving my abilities in scientific thinking, writing as well as presenting. He always gave his hand to me when I encountered unexpected obstacles, and encouraged me to rise from my dilemma, which led me to make such a great amount of research progress.

I would also like to thank my committee members, Prof. Chen Ji and Prof. Toshiro Tanimoto, and the research colleagues in ORCA experiment, Prof. James Gaherty and Joshua Russell, who have the attitude as well as the substance of a genius and gave me super useful suggestions in finding novel possibilities within my research work.

In addition, a thank you to all of my colleagues in the seismology office, who also did a lot of eye-catching research achievements. Our daily discussion really lighted my enthusiasm towards science and always brought me amazing brain storms. They also gave valuable comments and help to my research work, without which I will not be able to come up with these colorful research ideas.

ABSTRACT

Imaging Central Pacific Upper Mantle using P-wave Tomography and Receiver Functions

by

Lun Zhang

Several aspects of the oceanic lithospheric mantle remain unknown, largely due to the lack of dense local seismic instrumentation. In particular, we do not understand the nature of lithosphere-asthenosphere boundary, sparsely observed mid-lithospheric velocity gradients, and dynamic processes below the plate that may play an essential role in controlling Earth surface evolution. The Pacific OBS Research into Convecting Asthenosphere (Pacific ORCA) experiment included a ~1 year deployment of an 500x500 km^2 OBS array consisting of 30 stations in the central Pacific Ocean on ~40Ma seafloor northeast of the Marquesas Islands. Sub-lithospheric small scale convection (SSC) is a promising theory accounting for the observed gravity lineations at this area, although it has not been seismically imaged. Here we present results from the first year of ORCA data.

With teleseismic events $(30-95^{\circ})$, We measured differential travel times for P-waves from both vertical and pressure components using multi-channel cross-correlation. We combined these data and tomographically inverted for 3-D P-wave velocity structure. We find the alternating velocity anomaly bands oriented in WNW-ESE direction, which is nearly parallel to the gravity lineations, offering potential support for the presence of SSC. The depth range of that anomaly is ~150-250km based on a squeezing test. We also used events over

Mw6.0 to calculate P-s receiver functions (RF). After conversion multiple/water phase removal using a FIR filter, the RFs were migrated to image deep discontinuities using a CCP stack. The result revealed ~50-60km deep negative velocity gradient (NVG) which still needs to be tested by data from the latest deployment.

TABLE OF CONTENTS

I. Introduction 1

II. Background 2

A. Scientific motivation 2

B. Hypothesis – Small scale convection 4

III. Research 6

A. Experiment and data 6

1. Experiment overview 6

2. Data anomaly identification and removal 8

3. Sensor ball drop detection 9

4. Vertical record cleaning 11

B. Receiver function (RF) analysis 12

1. RF calculation and culling 13

2. Crustal multiple/water phase removal and CCP migration 15

C. P wave tomography 19

1. Differential travel time measurement 20

2. Tomographic inversion 23

3. Resolution test and depth constraint 28

IV. Discussion 32

V. Conclusion 34

References 35

I. Introduction

Traditional plate tectonic models fail to explain several aspects of the oceanic lithosphere. For instance, widespread off-axis, non-plume volcanism is observed on the Pacific plate, but the origin of this igneous activity is not understood. The depth-age relationship predicted by traditional plate cooling model breaks down in old (>80 Ma) ocean plates with anomalous seafloor shallowing. These phenomena may be explained by small scale convection (SSC) in the oceanic asthenosphere. In SSC theory, as oceanic lithosphere cools density increases, until the lower portion becomes gravitationally unstable, founders, and is replaced by warm asthenospheric mantle. Although the existing gravity observation fits well with SSC prediction, SSC has not been directly imaged in the oceanic upper mantle at this scale. To test the SSC theory as well as further study the structure and evolution of the oceanic plates, using teleseismic data from the Pacific OBS Research into Convecting Asthenosphere (Pacific ORCA) experiment the upper mantle beneath central Pacific Ocean will be seismically imaged.

II. Background

A. Scientific motivation

Although the hot spot theory succeeds in predicting the formation of some age-progressive volcano chains (Morgan et al., 1972), it fails to explain a lot of off-axis volcanism especially on the Pacific plate, which doesn't clearly show a linear age-distance relationship as expected (Ballmer et al., 2009; Sandwell et al., 1995). As shown in Fig. 1, the large distance spans of nearly coeval volcanism are hard to reconcile with hot spot theory, which predicts a more linear age-distance relationship (Ballmer et al., 2009). Thus an alternative hypothesis is needed.

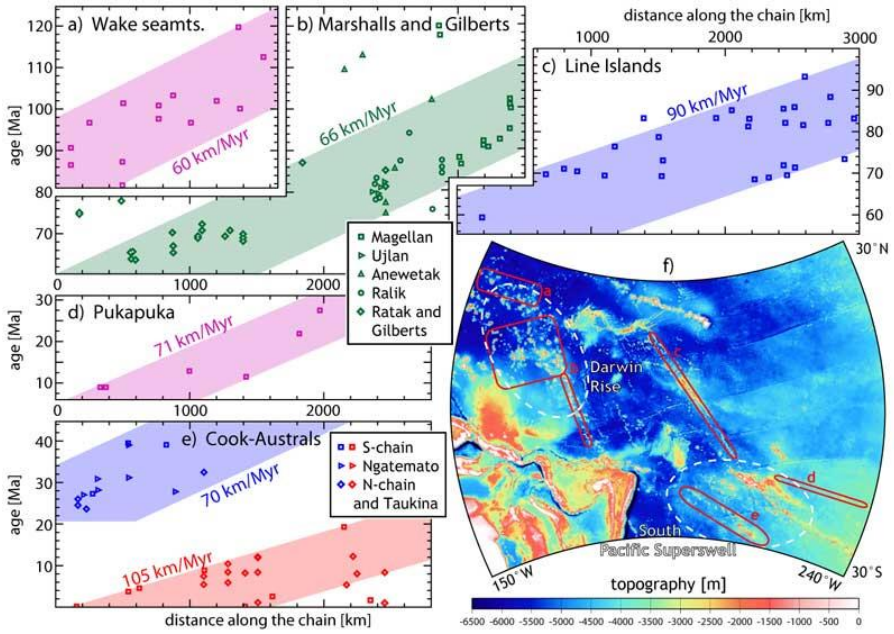

Figure 1. Ages collected at (a) the Wake seamounts, (b) the Marshalls, (c) the Line Islands, (d) the Pukapuka ridges, and (e) the Cook-Australs plot within fields in age-distance space of widths 1500 km (Figures 1a, 1b, and 1e), 2000 km (Figure 1c), and 1000 km (Figure 1d) with slope roughly equal to plate motion velocity. (f) Positions of the volcano chains on the Pacific Plate. (Ballmer et al., 2009)

Pacific oceanic lithosphere also exhibits certain unexplained trends as a function of age. Either half-space or plate cooling model predicts a decaying seafloor depth-age curve

(Turcotte and Schubert, 2014), but observations show that it breaks down in old (>80 Ma) ocean plates (see Fig. 2(a)) with anomalously high seafloor topography and heat flow (Crosby et al., 2006; Parsons and McKenzie, 1978; Parsons and Sclater, 1977; Stein and Stein, 1992) between ~80 and ~130Ma. This shallowing can not be directly explained by any traditional cooling model alone.

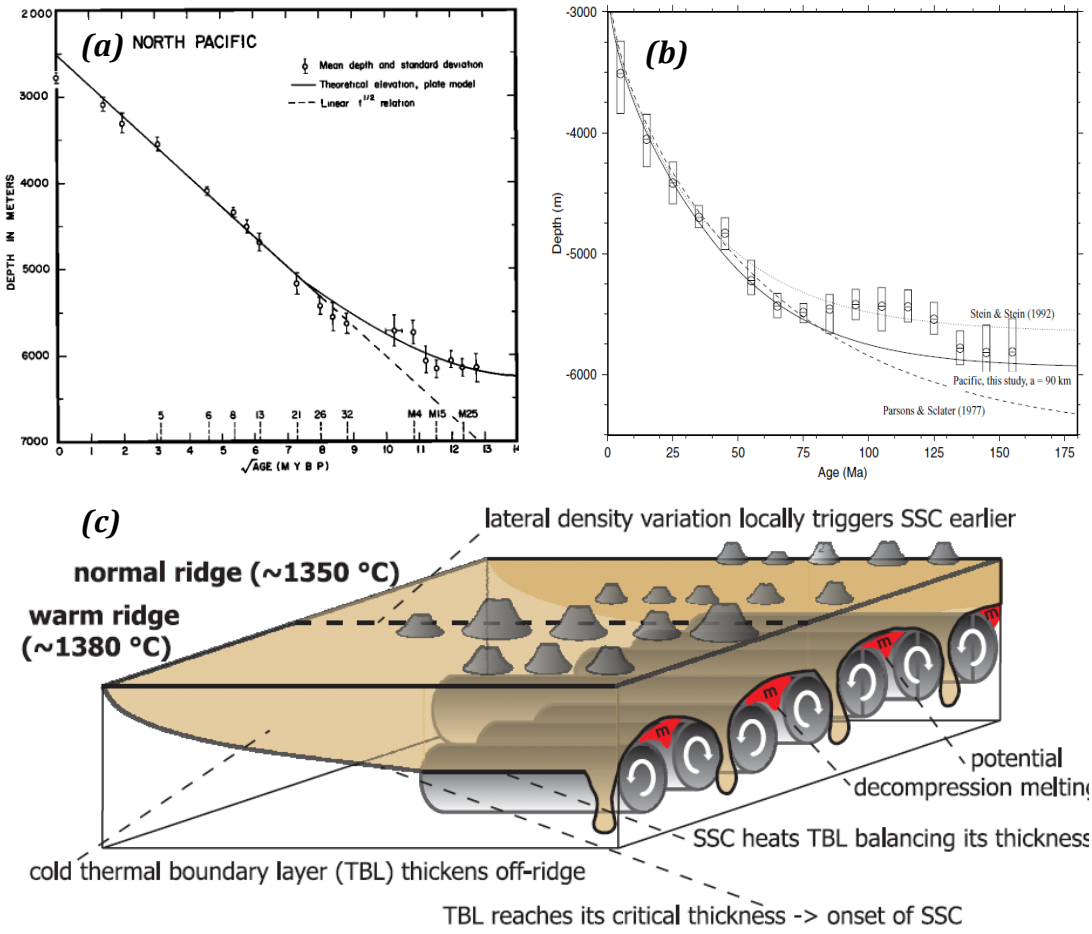

Figure 2. (a) Plot of mean depth in the North Pacific versus the square root of ages (Parsons and Sclater, 1977), dashed line is the depth-age relationship predicted by half-space cooling, solid line is interpolated from observations. (b) A comparison between best-fit theoretical depth-age relationship of Parsons and Sclater (1977) (dashed line), Stein and Stein (1992) with sediment thickness corrected (dotted line) and Crosby et al. (2006) with anomalous topographic measurements rejected (solid line). (c) Schematic plot of SSC mechanism. SSC spontaneously evolves at the bottom of mature oceanic lithosphere (Ballmer et al., 2009).

Study of non-plume volcanism formation as well as plate cooling mechanisms can

improve our understanding of oceanic lithospheric properties the evolution on Earth's surface.

B. Hypothesis – Small scale convection

Sublithospheric small scale convection (SSC) is a very likely mechanism for non-plume oceanic volcanism formation (Ballmer et al., 2007; Buck, 1985; Haxby and Weissel, 1986). It takes the form of convective rolls aligned with APM (Richter and Parsons, 1975). SSC spontaneously develops in the upper mantle due to the instabilities at the base of lithosphere whenever its thickness exceeds the critical value (Ballmer et al., 2007). SSC can change the thermal and compositional stratification in the upper mantle, allowing decompression melting and formation of volcanism (Hernlund et al., 2008). The duration of such melting is dominated by asthenospheric cooling. Ballmer et al. (2009) predicted a duration of 10–20Ma using 3D finite element simulation. The melting is elongated (a "hot line") instead of occurring at a fixed point like a hot spot, making associated volcano chains not age-progressive in any simple sense. Fig. 2(c) shows a schematic diagram of SSC developed beneath oceanic lithosphere.

SSC can also provide a natural explanation for the oceanic plate aging problem. Parsons and McKenzie (1978) suggested that the depth-age curve flattening is caused by the additional heat from convective instabilities in the thermal boundary layer (TBL). They tested this process using theoretical local Rayleigh number criterion, and demonstrated that SSC is likely to develop after the onset of instabilities within the TBL. SSC helps to maintain a constant temperature structure at the base of the plate and thus a stable maximum plate thickness less than predicted from half-space cooling. Crosby et al. (2006) also proposed that the anomalous bulge between 80Ma and 130Ma for north Pacific age-depth observations can be explained by the mantle upwelling stage of such convection cycle.

To date, the most powerful evidence for SSC is still the widespread gravity lineations

aligned in APM direction, typically with the wavelength comparable to SSC prediction as shown in Fig. 3(a) (Buck, 1985). Haxby and Weissel (1986) first discovered such gravity undulations from Seasat altimeter data and related them to gravity rolls induced by SSC. Although Sandwell et al. (1995) argued that ridges within free-air gravity lows is contradictory to expected gravity (and topography) highs in SSC model, Harmon et al. (2006) found that after removing the volcanic surface load and associated flexure the volcanic ridges are actually located on broad topographic highs, which is consistent with SSC prediction. Meanwhile, the free-air gravity and Bouguer anomaly lows along volcanic ridges could denote buoyant material in the upper mantle or crustal underplating (Harmon et al., 2006).

Although SSC theory can provide reasonable explanation for these two scientific questions, our knowledge about it is limited. The formation mechanism of volcanism at young ages is still debated; alternative explanations including lithospheric cracking, viscous fingering and asthenospheric shear-driven upwelling (SDU) can also account for both volcanism and observed gravity lineations (Ballmer et al., 2013; Harmon et al., 2011; Weeraratne et al., 2007), making the problem more complex. Although different hypotheses predict distinct seismic observations, differentiating them requires tomographic resolution of features <200 km in wavelength in the upper mantle – a level of resolution unattainable by global seismology. And if we assume SSC can account for non-plume volcanism formation at young ages, then it would be inconsistent with the fact that the anomalous bump of depth-age curve is only observed in older area, unless SSC beneath plates of different ages were to somehow differ in its characteristics (e.g., magnitude or scale). To address these uncertain points about SSC theory, I propose using OBS data from the Pacific ORCA experiment to seismically image the upper mantle structure beneath Pacific Ocean.

III. Research

A. Experiment and data

Seismic imaging resolution has been limited in the Pacific basin due to sparse island seismic station distribution. The 2018-2019 Pacific ORCA deployment of a 30-instrument array of ocean bottom seismometers (OBS) was designed to address this problem and allow high-resolution upper mantle imaging for testing the SSC hypothesis.

Below, I outline the data quality and availability, procedures to remove data anomalies, idiosyncrasies of this dataset's engineering issues, and pre-processing techniques applied to the OBS seismic data prior to analysis.

1. Experiment overview

The Pacific OBS Research into Convecting Asthenosphere experiment was designed to analyse two different locations within the Pacific basin that show evidence of SSC. In this research I will focus on the first region, ~40Ma lithosphere northeast of Marquesas Islands that was formed at the EPR, 2700 km to the ESE. This region was chosen for 2 reasons. On the one hand, gravity lineations with 140~200km wavelengths are evident in this area, which is comparable to SSC model prediction. On the other hand, satellite altimetry shows that there are no major volcanic ridges in our research region, so the volcanism effects on observations including bathymetry and the low velocity zone can be largely eliminated.

A 500x500 km^2 OBS array consisting of 30 seismic stations was deployed for around 13 months. The array was oriented orthogonal to the gravity lineations to span 2-3 wavelengths of the observed gravity rolls as shown in Fig. 3(a), with the goal of imaging convection rolls. The central linear 12-OBS subarray was designed to maximize body wave analysis resolution

and thus the SSC imaging quality.

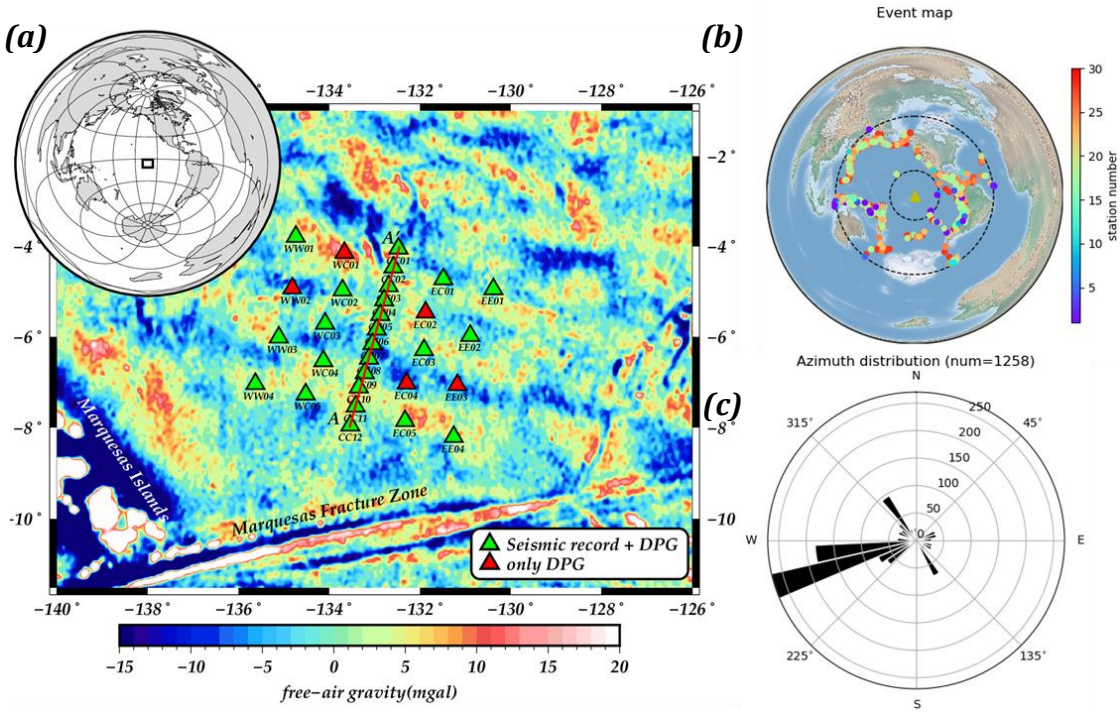

Figure 3. Deployment and teleseismic data availability. (a) ORCA OBS array (colored triangles) at ~40Ma seafloor northeast of the Marqueses Islands, overlapped on free-air gravity map, red line AA' denotes the selected profile for CCP imaging. (b) Distribution of events ($M_w \geq 5.0$, $30^\circ \leq distance \leq 95^\circ$), the yellow triangle represents central position of our research region, color of the scattered points denotes the number of stations recording a specific event. (c) Azimuthal distribution of events in (b).

From ~1 year 3-component ground motion time series as well as pressure record of OBS, I extracted as many teleseismic waveforms with clear seismic body wave phases as possible based on global USGS catalog. The waveforms after quality control were then used to calculate *P*-wave receiver functions and measure *P*-wave differential travel time for tomographic inversion. After data culling, on average each teleseismic $Mw \geq 5$ event was successfully recorded by over 20 stations (Fig. 3(b)), providing enough data for the applied seismic imaging techniques. The events are not evenly distributed by back azimuth; a majority come from the SW (Fig. 3(c)), which may cause potential bias in the inversion.

2. Data anomaly identification and removal

OBS data often contains some anomalous segments, which can be caused by various kinds of abnormal instrument states (e.g. releveling, power shortage) in the oceanic environment. The records within such segments are typically pure noise or comprise signal artifacts, so it is necessary to identify and remove these anomalies from OBS data. Here a power spectrum density (PSD) analysis was used to find those anomalous data segments automatically, then the probability density function (PDF) with noise baselines (McNamara et al., 2009) helps to check how well removal works.

From spectrograms of the entire OBS record, I identified 3 main types of anomaly including data gaps, data with flat power spectra, and data with extremely low amplitude (Fig. 4(a)). Certain regions of the PSD were identified as representative of anomalous data, and all of the records falling into those regions were rejected. Fig. 4(b) shows an example of PSDs before and after removal of data anomalies. This automatic analysis clearly removes anomalous linear spectra visible in seismic channels below 50dB. This quality control does not affect the overall PDF within the normative data window.

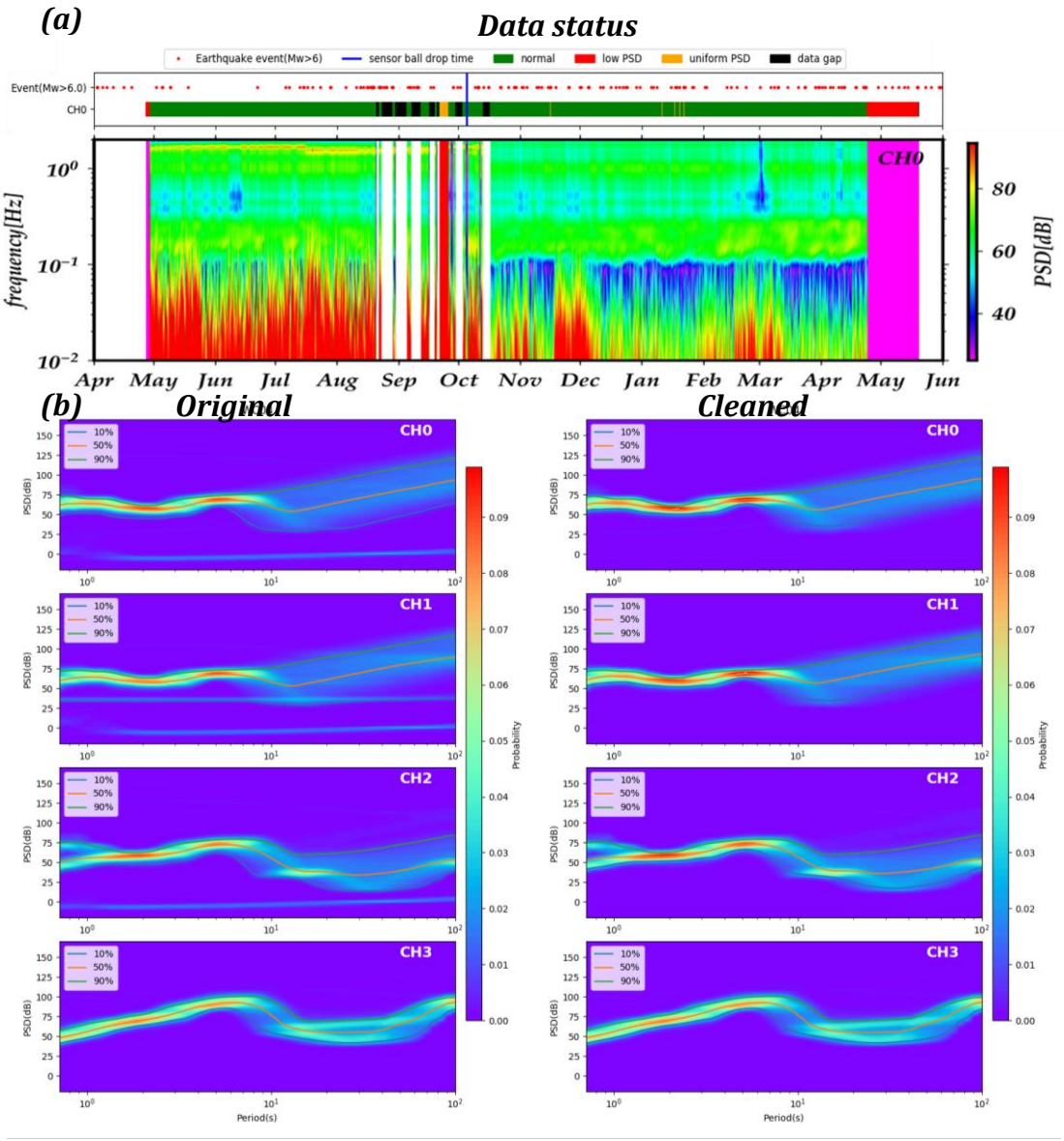

Figure 4. Figures showing data quality for station WC04. (a) Data status classification based on spectrogram. (b) PDF for station WC04 before (left) and after (right) data anomaly removal. CH0, CH1 – horizontal channel, CH2 – vertical channel, CH3 – pressure channel.

3. Sensor ball drop detection

For OBS in the ORCA deployment, developed by the Scripps Institution of Oceanography OBS group, the sensor ball was connected to an arm jutting out from frame. The sensor was designed to release from the arm via a mechanism that involves magnesium pins, which should

corrode 24-48 hours after first contact with seawater, at which point the sensor ball should detach from the OBS frame and land on seafloor. In response to previous safety issues or premature detachment, the OBS release mechanism for this deployment was re-designed to take the pins out of the load path of the sensor ball. While the new mechanism worked in bench tests, we have reason to believe it did not perform as expected on the seafloor. For seismic channels of several stations, the spectrogram shows an abrupt change in noise properties at the middle of deployment time. This change has two main features: (1) the stable noise peak within frequency band 1-2Hz which is likely to be OBS frame resonance abruptly disappears (2) current-induced noise (<0.1Hz) level dramatically decreases. Such change is most likely to be caused by the sensor ball drop. So for these stations, the sensor ball did not drop until the middle of the deployment. Knowing the exact drop time is important given the clear difference between data recorded by sensor ball in the hanging versus the dropped state.

I designed a method based on coherence analysis to automatically search for OBS drop time. This method exploits the fact that while the OBS is hanging there is high correlation between vertical and horizontal motions. For each date, the variation of average H(Horizontal)-Z(Vertical) coherence within frequency band 1-2Hz is calculated, taking the form of difference between the average daily coherence over the 30-day window before and after the date. If the maximum H-Z coherence drop is over a (empirically-determined) threshold value, it indicates a sensor ball drop event, which is then determined to have occurred on the date with maximum H-Z coherence drop. Fig. 5 exemplifies the coherence difference between hanging and dropped state of the sensor ball. After the sensor ball drop, it is clear that (1) resonance (>1Hz) coherence for H-Z is largely eliminated (2) compliance (peaking at ~0.01Hz) coherence for P-Z dramatically increases (3) current-induced noise

(<0.1Hz) coherence for H-Z relatively decreases.

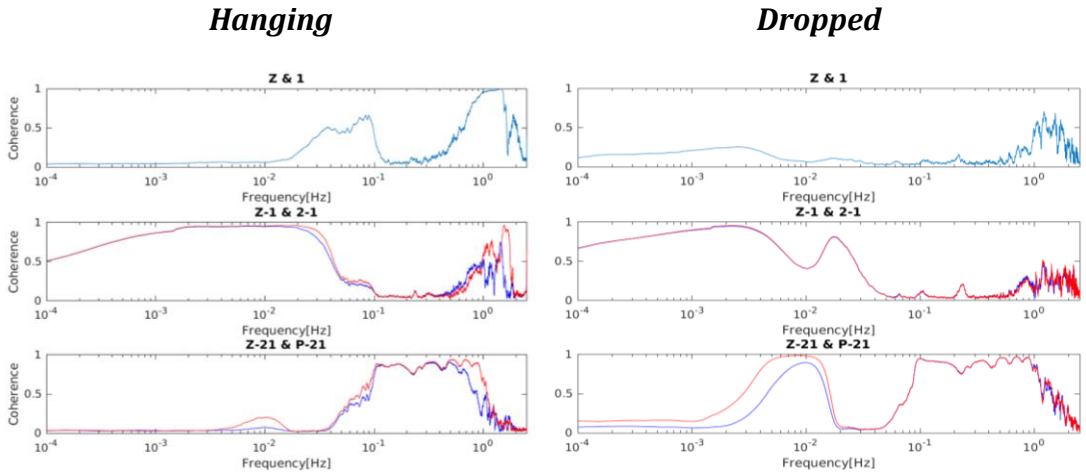

Figure 5. Average coherence between different components for hanging (left) and dropped (right) state, the example station is WC04. Z – vertical channel, 1, 2 – horizontal channel, P – pressure channel. Blue line shows coherence calculated using original records, red line shows coherence calculated using cleaned records.

4. Vertical record cleaning

The vertical record is contaminated by both compliance and current-induced tilting noise. This noise can obscure useful signals in the data. In this research, to recover as many body wave phases as possible, low-frequency oceanic noise was removed by calculating transfer functions between vertical and pressure (for compliance) as well as vertical and horizontal components (for tilt) (Crawford and Webb, 2000). An example effect of such cleaning is shown in Fig. 5 and Fig. 6(a), after removing the coherent effect from horizontal components, we find a rise in P-Z compliance coherence, which was previously suppressed by current-induced noise. Fig. 6(b) shows the example for an earthquake event waveform correction.

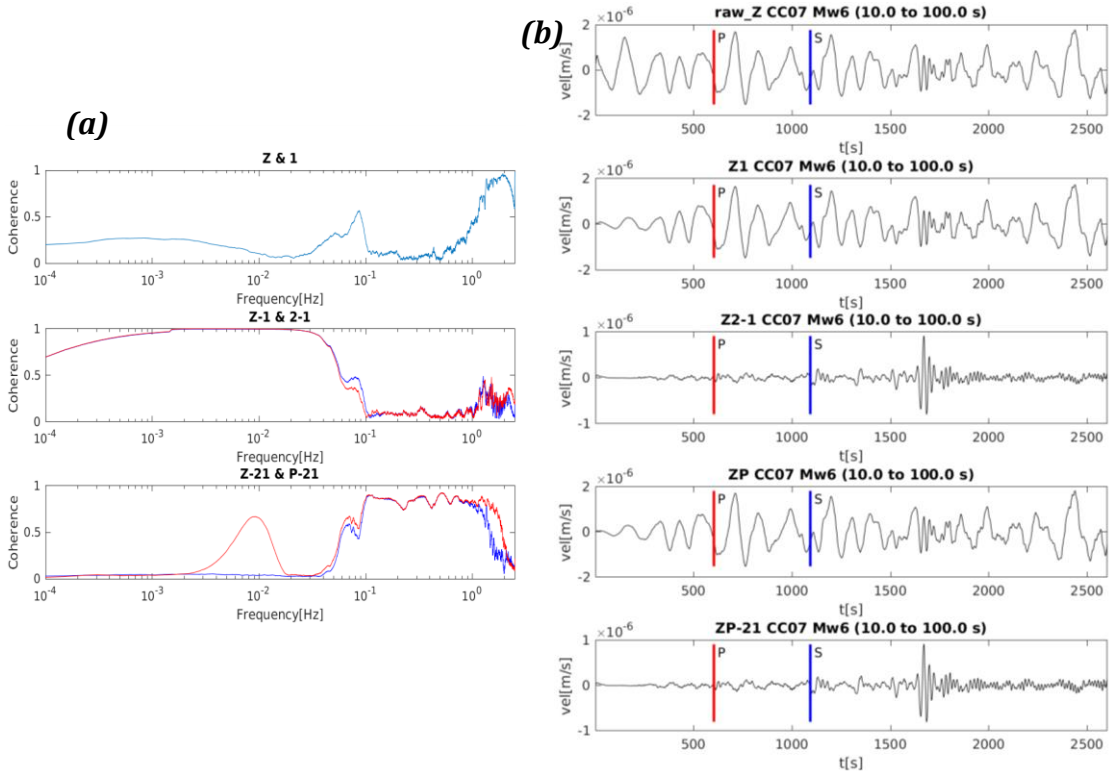

Figure 6. Example station is CC07. (a) Average coherence between different components. (b) Seismic waveform correction example, time is relative to event origin. Z1 – only use H1 (CH1) as source component to clean Z (CH2), Z2-1 – firstly use H1 (CH1) and then H2 (CH0) as source component to clean Z (CH2) in order, ZP – use P (CH3) as source component to clean Z (CH2), ZP-21 – use H1 (CH1), then H2 (CH0), then P (CH3) as source component to clean Z (CH2) in order.

B. Receiver function (RF) analysis

P-wave receiver functions (RFs) can be extracted from 3-component teleseismic records through deconvolution. This method is widely used to study crust and upper mantle structure by providing sensitivity to gradients in seismic velocity. Since seismic records of OBS are very noisy, we will explore use of a variety of culling techniques to improve the final RF quality. Based on robust data, a series of existing imaging tools associated with RFs can then be applied to explore various aspects of the sub-surface.

1. RF calculation and culling

An essential step in calculating RFs is to rotate the 3 seismic components to RTZ coordinates, requiring knowledge of the OBS horizontal channel orientation. To determine this orientation, I adopted the method of Stachnik et al. (2012), using Rayleigh wave polarization measured from multiple earthquakes (Fig. 7). The final orientation result is stable and does not show dependence on event azimuth or time. The particle motion in the rotated RZ plane within the Rayleigh wave interval mostly shows perfect retrograde elliptical orbit, demonstrating the accuracy of station orientation found by this method and the quality of our data.

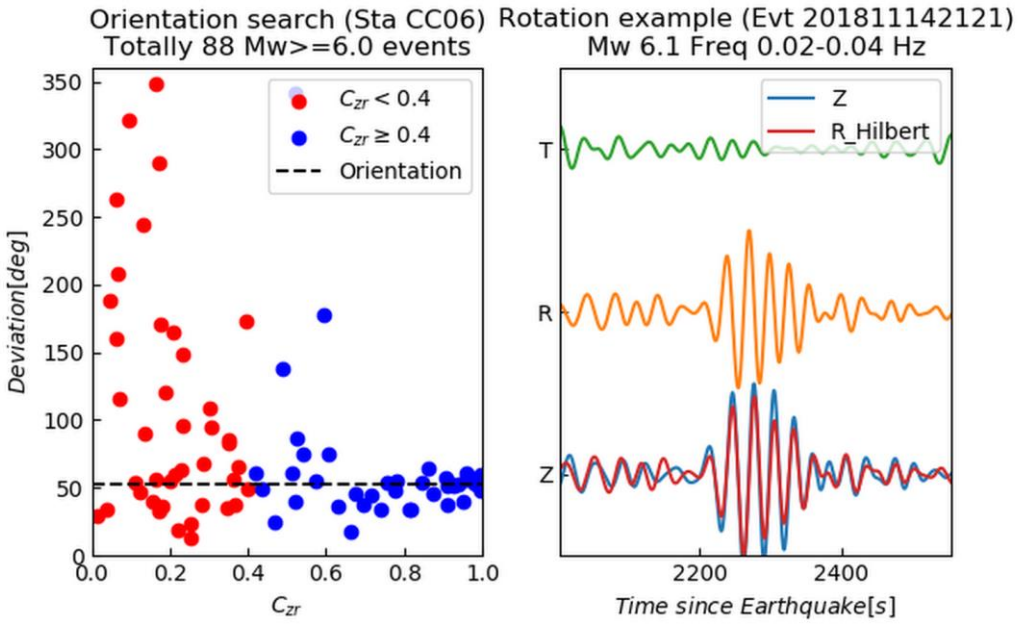

Figure 7. Figure showing orientation determination from all available earthquakes (left) and component rotation for a single earthquake arrival (right) for station CC06. After rotating the ZNE components with orientation determined through the method of Stachnik et al. (2012), within the Rayleigh wave interval there seems to be little energy on transverse component but strong energy on the radial as well as vertical component, meanwhile the Hilbert transform of radial record fits well with vertical component, demonstrating the that the data correspond to a well-recorded Rayleigh wave, with properly corrected station orientation.

Taking the vertical component as parent trace, and radial component as daughter trace, I

calculate RFs for each station based on time domain iterative deconvolution (Ligorría and Ammon, 1999). RFs of our OBS are noisier compared with typical RFs at land stations. Directly stacking inconsistent RF waveforms without first removing anomalous RFs shows conspicuous problems. For instance, important seismic phases reflecting real structures are depressed or even overwhelmed and unexpected artifacts are introduced. To reliably reject improper waveforms, I developed a 3-step culling procedure (Fig. 8(a)-(c)).

Firstly, RF waveforms with too high (>1) or too low (<0.1) parent phase amplitude are rejected. Secondly, a template RF waveform is constructed from all of the rest waveforms based on principal component analysis dimension reduction, which is expected to reflect the primary pattern of the RFs. The cross-correlation coefficient is calculated between this template and each individual waveform; those with low coefficients (<0.4), which deviate substantially from the primary pattern are rejected. Finally, the remaining RFs are checked by eye for anomalies that are not recognized before. Fig. 8(d) shows effects of such RF waveform culling and stacking, with a comparison to a theoretical RF waveform modeled using a simple 2-layer model (including Moho). After culling, the major phase amplitudes of stacked RFs seem to be more comparable with those of synthetics.

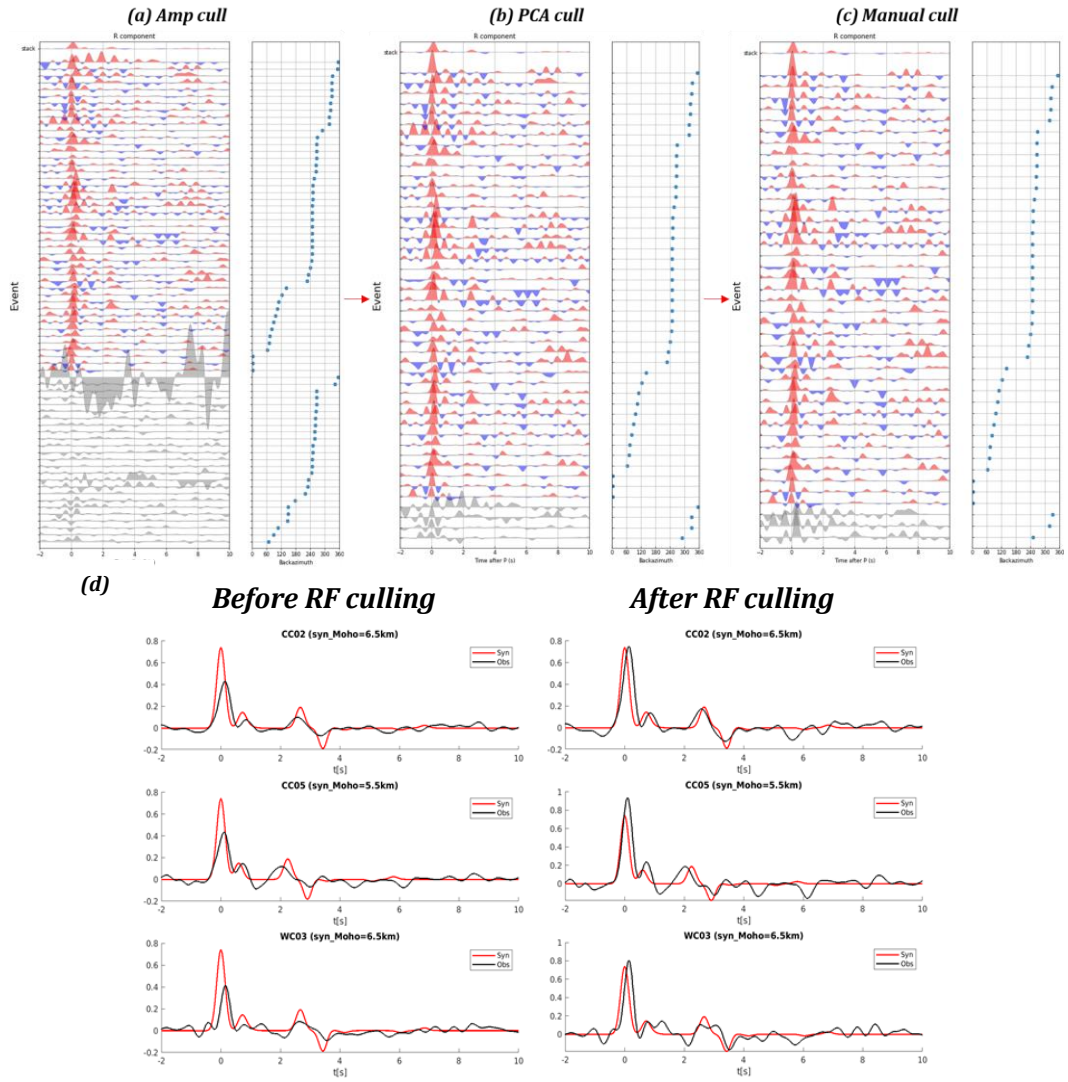

Figure 8. The frequency band of RFs calculated were 0.1-2Hz. (a)-(c) 3-step RF culling process for station CC02. The grey waveform means RFs rejected through certain types of culling step. (d) Example stacked RFs before (left) and after culling (right), red waveform is synthetic RF with a simple 2-layer model, black waveform is the stacked RF.

2. Crustal multiple/water phase removal and CCP migration

In *P*-wave receiver functions, the phases generated from mantle structure like the lithosphere-asthenosphere boundary (LAB) may be masked by crustal reflection multiples as well as water reverberation phases (Olugboji et al., 2016). Mantle structure plays a key role in testing SSC theory, so it is important to eliminate effects of crustal multiples as well as water signals and recover true mantle phases. I designed a method for crustal multiple/water

phase removal based on RF modelling.

For the case of crustal multiple removal, we approximate the Moho response on the RF waveform as a transfer function. Given the correct Moho properties, deconvolving this transfer function from the observed RF should remove the crustal phases in the data. To implement this process, I modeled the synthetic RF waveform using the propagator matrix approach (Kennett, 1981), then the transfer function was obtained by the spectral division of the result obtained from the 1-D crustal model and the result obtained from the 1-D model without Moho. The success of crustal phase removal largely depends on the applicability of the 1D crustal model used. If the synthetic crustal properties match the true crustal properties, the Moho response will be correctly removed. A grid search was conducted to find the combination of Moho depth, *H(4.0-8.0km)*, as well as crustal average *S*-wave velocity, *Vs (3.2-4.2km/s)*, that best removed crustal phases through searching for the parameters that minimize the objective function which is the 1_{st} norm of the corrected waveform within 2-4s. For this modelling, crustal *P*-wave velocity, density and mantle properties are set as default values. Fig. 9(a) shows an example for crustal multiple removal. After deconvolving the crustal transfer function simulated with the best (*H*, *Vs*) pair, the crustal phases are clearly removed from the original stacked receiver function.

In order to remove the water multiples, a similar approach was applied, except that the water sound speed and depth is already known. I replaced the synthetic crustal model with a water column at the top of the model with height and Vp determined from local acoustic site surveys processed with the OBSrange software (Russell et al., 2019). The water signals should be theoretically removed after deconvolving the synthetic water column response. Fig. 9(b) shows an example for water phase removal. Interestingly, there seems to be a ~0.5s shift

between the negative phase at 5.5-6s and theoretical 1st water reverberation signal arrival, as a consequence, the final cleaned RF doesn't seem to totally exclude this negative phase but generate a 'doublet' between 5.5-6s.

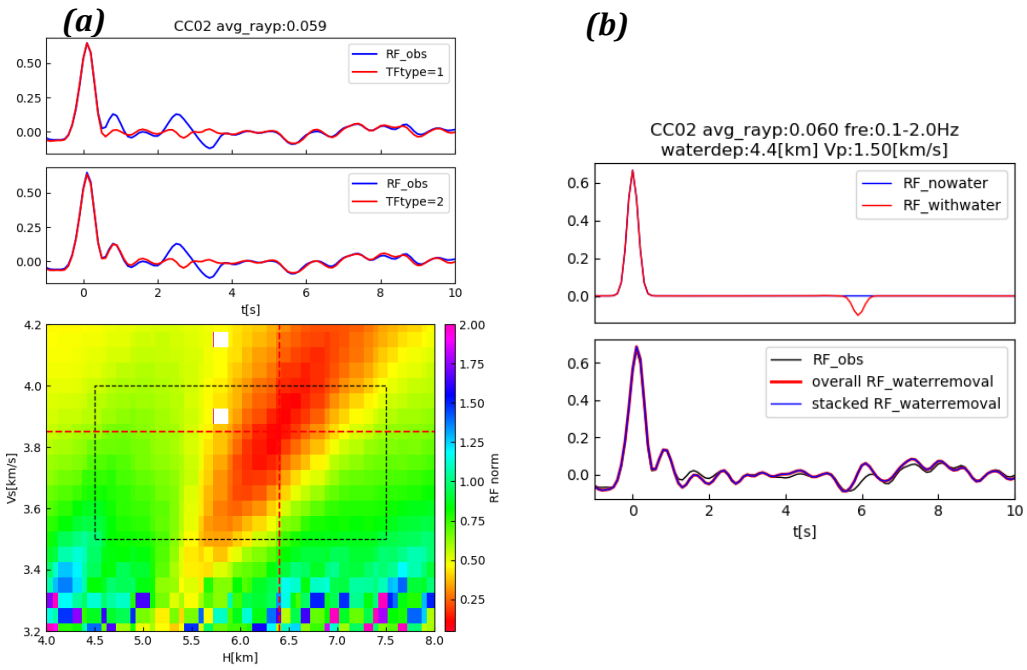

Figure 9. All the operations were within the frequency band 0.1-2Hz, Q was set as infinitely high so attenuation effect was not taken into account here. (a) RF crustal multiple removal process for station CC02. Bottom: Grid search for finding best (H, Vs) to synthesize crustal response. The objective function is the norm of cleaned RF segment between 0.5s and 4s (for ruling out parent phase). Top and middle: RF cleaned (red) with 1st (removes all crustal phases) and 2nd type of transfer function (removes crustal multiples but retains Ps phase) respectively and original stacked RF (blue). (b) Water phase removal process for station CC02. The top plot shows synthetics generated from a uniform model with/without a water column sitting atop, which were used to calculate the water column response. The bottom plot shows the stacked RF without crustal multiples (black) and RF with water phases removed, 'overall RF_waterremoval' was obtained by applying the correction directly to stacked RF, while 'stacked RF_waterremoval' was obtained by stacking individual RFs with water phase corrected independently.

Common conversion point (CCP) migration and stacking (Zhu, 2000) was then applied to locate subsurface interfaces. RFs were backprojected to their assumed conversion points, determined by ray tracing in a crust-modified IASP91 model. The phases were stacked onto a 2-D profile parallel to the dense central line of OBS. Some notable features spanning the entire

research area are visible after masking RF amplitudes below 0.1. In the CCP profile using original RFs (Fig. 10(a)), we observe a strong positive velocity gradient interface at ~6km. This is most likely to denote the Moho discontinuity. We also observe continuous positive and negative phases between 20-40km – these are the crustal multiples, artificially projected into the mantle. The strong negative phases observed between 50-60km depth are also quite stable and laterally continuous, but these phases seem to overlap with migrated water phase depth, which means they could be at least partly attributed to the water multiples. In the CCP profile using corrected RFs (Fig. 10(b)), the crustal multiples are largely eliminated between 20-40km depth and the real mantle structure is theoretically recovered. There seems to be little laterally continuous features in the 20-40 km depth range. After deconvolving predicted water signals from RFs, a considerable part of negative phases between 50-60km depth was still retained, which could indicate potential layer with negative velocity gradient (NVG) at that depth. It is not that clear whether the negative phases between 50-60km were totally caused by water reverberation or they were a combined effect of both water phase and phase generated from mantle gradients. A promising way to resolve this would be to look at oldORCA data where the deeper average water depths will induce different timing of the water reverberation, potentially allowing us to discriminate these signals.

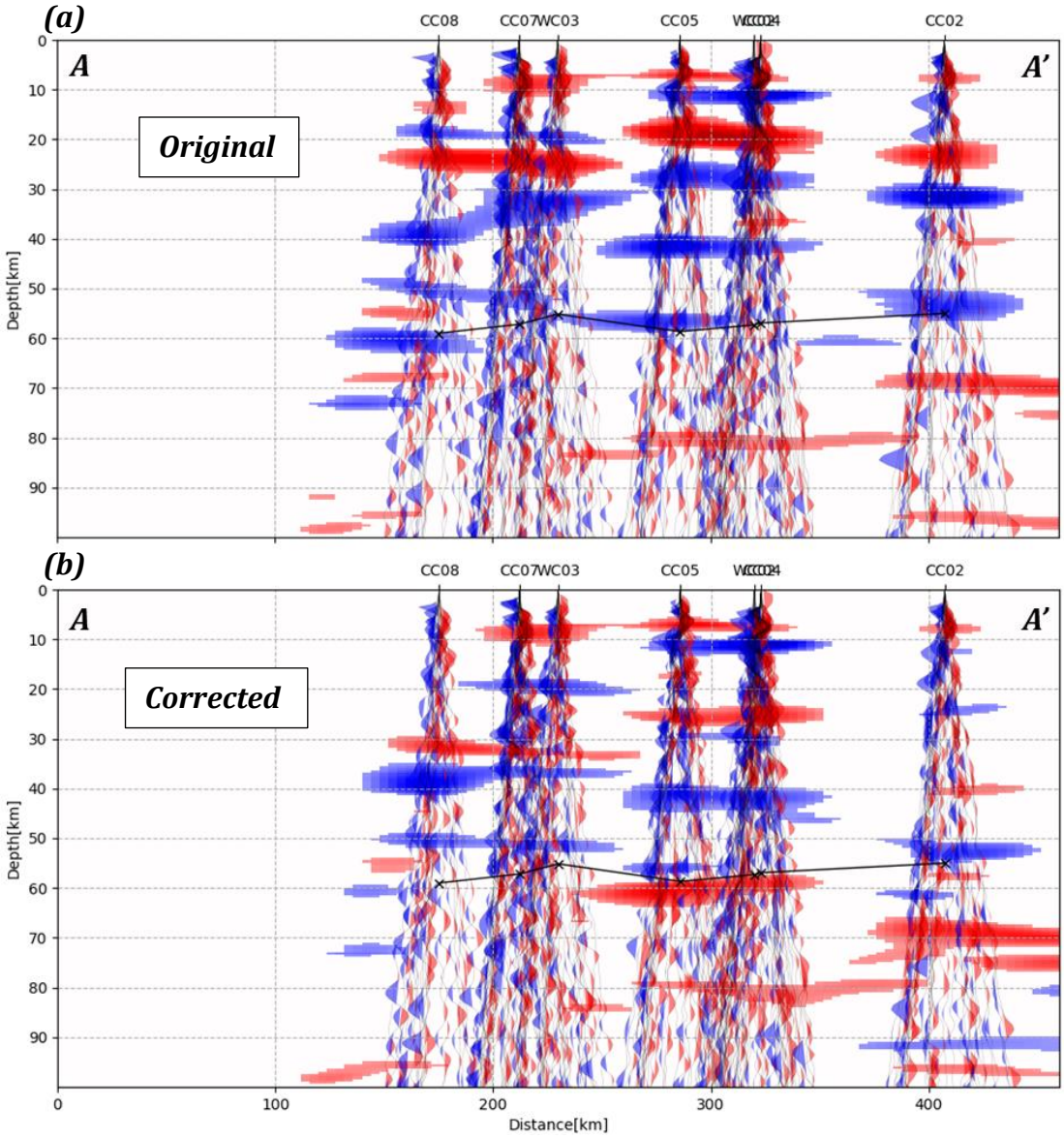

Figure 10. CCP migration imaging along profile AA' defined in Fig. 3. Seismic ray curves (based on crust modified IASP91 model) with RF amplitude projected on the selected profile, the frequency band is 0.1-2Hz. As for the background map, only the area with stacked amplitude over 0.1 was retained to make the primary features stand out. Black solid line and crosses denotes migrated depth of the theoretical 1st water reverberation signal peak, which is used to assist feature interpretation. (a) CCP profile using original RFs (b) CCP profile using RFs with crustal multiples and water phase removed.

C. P wave tomography

Teleseismic *P*-wave tomography is widely used in mapping upper mantle velocity structure. Using relative *P*-wave arrival times derived from OBS vertical as well as pressure

data, an ACH (Aki, Christofferson and Husebye) tomographic inversion (Aki et al., 1977) with finite frequency sensitivity kernels (Schmandt and Humphreys, 2010) will be conducted to reveal the 3-D *P*-wave velocity heterogeneities beneath our research area.

1. Differential travel time measurement

For each event, the relative arrival times of direct teleseismic ($30^\circ - 95^\circ$ distance) *P*-phase recorded across the array were measured through multi-channel cross-correlation (MCCC) (VanDecar and Crosson, 1990). This method uses a least-square inversion scheme to compute relative arrivals from the cross-correlation pairs, reducing multi-path effects as well as the requirement for waveform similarity. Given OBS data quality issues, I implemented an interactive approach to adaptively adjust the time window (which is around -5-3s on average) as well as filter frequencies used to involve the prominent direct *P*-wave signal in the cross-correlation, and reject bad traces based on several criteria including signal-to-noise ratio (SNR), *P*-wave amplitude and waveform similarity (determined by eye or cross-correlation coefficient with reference waveform). This method was applied to both vertical (Fig. 11(a)) and pressure (Fig. 11(b)) channels to measure differential *P*-wave travel times independently. These two types of traces were generally filtered in 0.3-0.6 Hz and 0.4-2Hz respectively to avoid the effects of noise (microseism, anomalous sensor noise, etc.). Fig. 13(a) and (b) shows the distribution of relative times measured on vertical and pressure channels respectively.

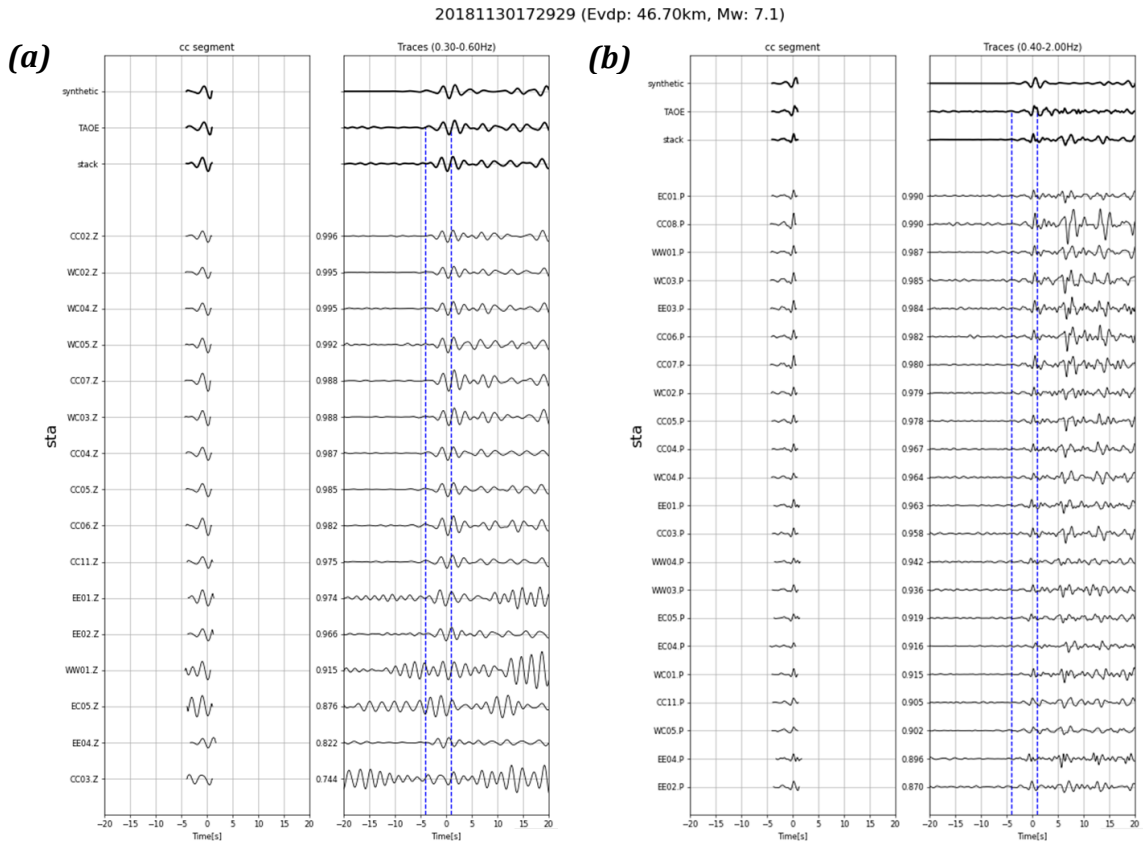

Figure 11. Interactive MCCC example for event 201811301729 in vertical channel (a) and pressure channel (b). Left column: post-alignment trace segments for cross-correlation. right column: pre-alignment traces. Time interval within blue lines was used to conduct MCCC. Here the synthetic from Syngine, seismic record from ~600km away land station TAOE as well as the stacked trace were used as reference waveform for assisting interactive trace culling, note that the polarity of synthetic and TAOE waveform was flipped so that they would be comparable to pressure waveform.

The MCCC processes for vertical and pressure traces are totally independent, but it is also possible to combine their differential *P*-wave travel time measurements to maximize the data for tomographic inversion. Here two types of combination approach were adopted. The first is 'direct combination' (termed '*PZdirect'* in the figures): if both vertical and pressure measurements are available for a given event, then only measurements from the channel with more usable traces are retained. The second is 'mixed combination' (termed '*PZmix'*), where the G matrix for MCCC on each event was reformatted using cross-correlation pairs from both

channels (using the fact that the differential P-wave arrival time is the same on both components of a single station). The final inverted differential travel time measurement is thus a combination of the individual channels' data (Fig. 12), incorporating maximum information from both datasets. Fig. 13(c) and (d) shows the distribution of relative times measured from direct combination and mixed combination datasets respectively. Considering ray coverage and the precision, among the 4 datasets we obtained before, the 'direct combination' is the preferred one based on whose tomographic model the main interpretation would be made.

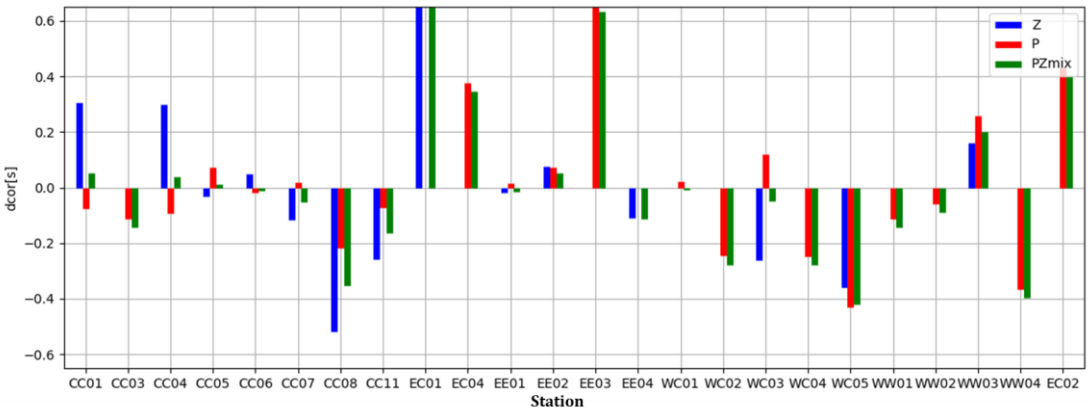

Figure 12. Comparison between single-channel and mixed combination differential *P*-wave travel time measurements for event 201809162111. Z – Vertical (BHZ), P – Pressure (BDH), PZmix – mixed combination. For each station, the relative arrival time estimated from the mixed MCCC approach is a trade-off between the two single-channel results.

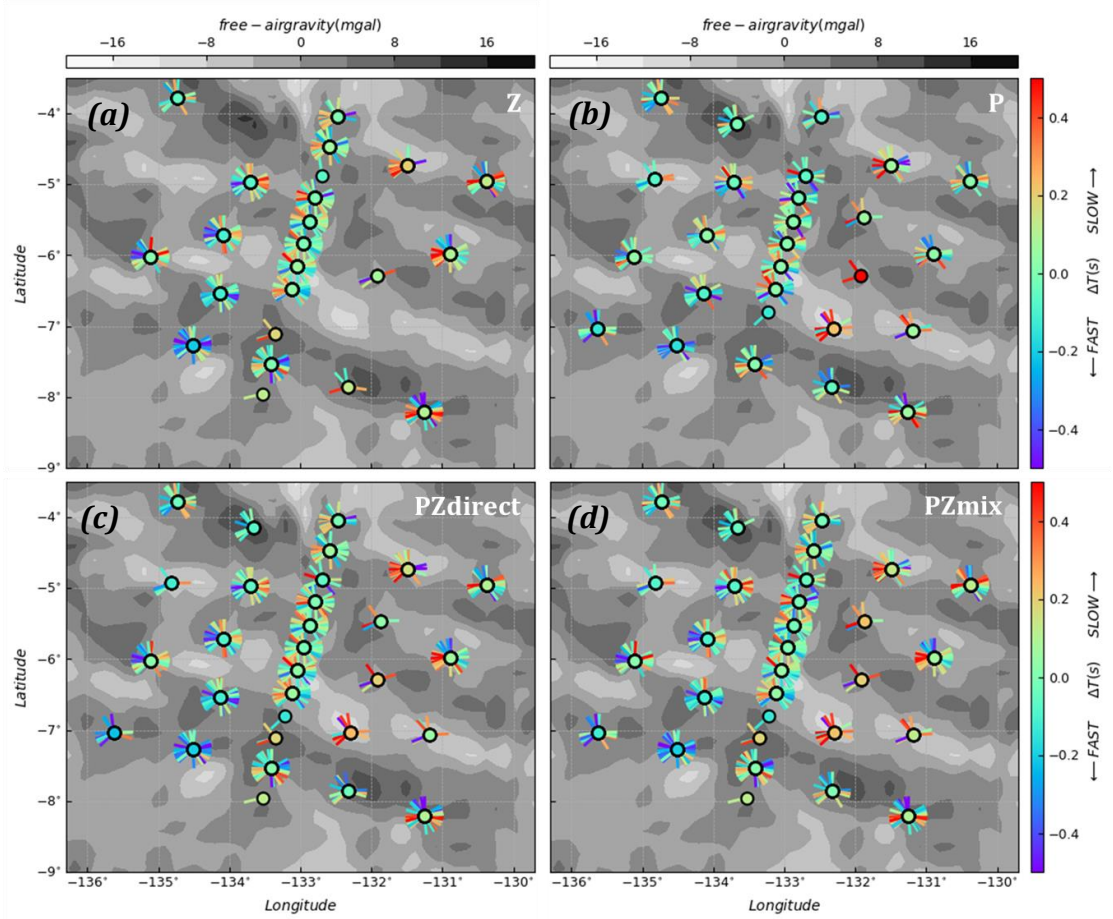

Figure 13. Geographic distribution of differential P-wave travel time measurement for single-channel (vertical (a), pressure (b)) and combination (direct (c), mixed (d)) datasets, spokes denote event azimuth, circles at station locations indicate its averaged relative arrival time.

2. Tomographic inversion

The differential traveltimes were then inverted for the slowness model using a finite frequency *P*-wave traveltime tomography. The model nodes are regularly spaced at 30km laterally, considering body wave sensitivity as well as our interested features we set the depth range as 6-300km with uneven vertical spacing as shown in Fig. 19(a).

The spatial coverage of data was described by “hit quality” parameter (Schmandt and Humphreys, 2010), which is calculated as the number of seismic rays in each voxel from each back-azimuthal hexant (saturating at a maximum of 6 rays per hexant, giving a total score out

of 36 that is normalized to a value between 0 and 1) and was assigned to each node of the model to indicate its resolvbility.

We applied both model norm damping and 1st derivative smoothing to regularize the inverse problem, which minimizes the following cost function:

$$E = \|w(Gm - d_{obs})\|^2 + \gamma\|\nabla m_0\|^2 + \epsilon\|m_0\|^2 + \epsilon_{evt}\|estatic\|^2 + \epsilon_{sta}\|sstatic\|^2 \quad (1)$$

where $G = [G_0\ G_e\ G_s]$, $m = \begin{bmatrix} m_0 \\ estatic \\ sstatic \end{bmatrix}$.

In the expressions above, m_0 is the vector of fractional perturbations to the initial slowness model, $estatic$ is the vector of event static time, $sstatic$ is the vector of station static time, d_{obs} is the vector of differential travel times, and G_0 is the matrix with$[G_0]_{ij} = \partial d_i/\partial[m_0]_j$, G_e is the matrix with $[G_e]_{ik} = \delta_{eid(i),k}$ ($eid(i)$ represents index of the event corresponding to i_{th} seismic ray), G_s is the matrix with $[G_s]_{il} = \delta_{sid(i),l}$($sid(i)$represents index of the receiver station corresponding to i_{th} seismic ray), w is a diagonal matrix of data weights, γ is the smoothing parameter, ϵ is the damping parameter for slowness model, ϵ_{evt}, ϵ_{sta} is the damping parameter for event and station static time. In this research, ϵ_{evt}, ϵ_{sta} is set to be 0.01 and 1 respectively, data weight is designed as the inverse of standard deviation calculated during MCCC process (VanDecar and Crosson, 1990).

The regularization was designed to balance data fitness, model norm and roughness, for which an adapted L-test was applied to search for optimal parameters. We analyzed the trade-off between X and weighted data variance reduction wvr (Fig. 14(a)) through minimizing the penalty function $\chi = X + F(1 - wvr)$ where F is an alterable factor adjusting the weight of X and wvr (Fig. 14(b)). We introduced X as the combination of model norm and roughness, $X = nval(||m||)/10 + nval(||\nabla m||)/dh$ where "nval" means the normalized value

compared to the maximum during the grid search in ϵ $(0-10)$ and γ $(0-10)$ $space$, and dh is the model spacing. Such tests suggested that $\epsilon = 2, \gamma = 5$ should be suitable regularization parameters for inversions using all 4 types of datasets.

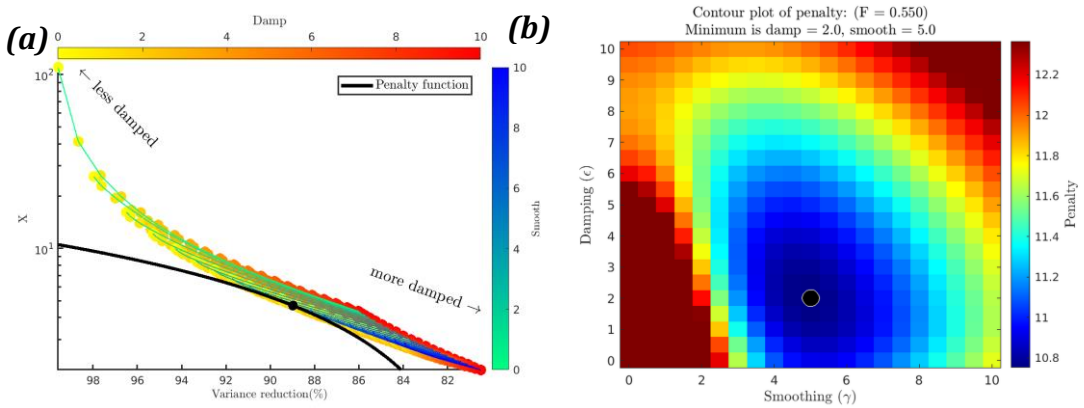

Figure 14. Example of determining optimal regularization using 'direct combination' measurements. The black dot denotes optimal regularization parameters found. (a) The curve showing trade-off between X and variance reduction (b) contour plot of penalty function, the F value was chosen empirically to guarantee reasonable regularization.

The inverse problem was solved through LSQR algorithm to minimize E in Equation (1). Fig. 15 shows the 3D tomographic imaging results for 4 datasets. The most significant result was that roughly $\pm 2.5\%$ P-wave velocity anomalies were observed between 180-300 km depth for all 4 models, taking the form of alternating flipped velocity anomaly bands in vertical channel and 2 combined-channel models between 220-260 km depth. These bands were aligned in WNW-ESE direction which was nearly parallel to the local gravity lineations.

The pressure channel model only shows limited anomalies consistent with other models, which is perhaps due to limited ray coverage. But a clear correlation between 2 single-channel model can be found by comparing their model values at nodes with high 'hit quality', which demonstrates the reliability of tomographic inversion we conducted given their independent datasets as well as differential travel time measurements.

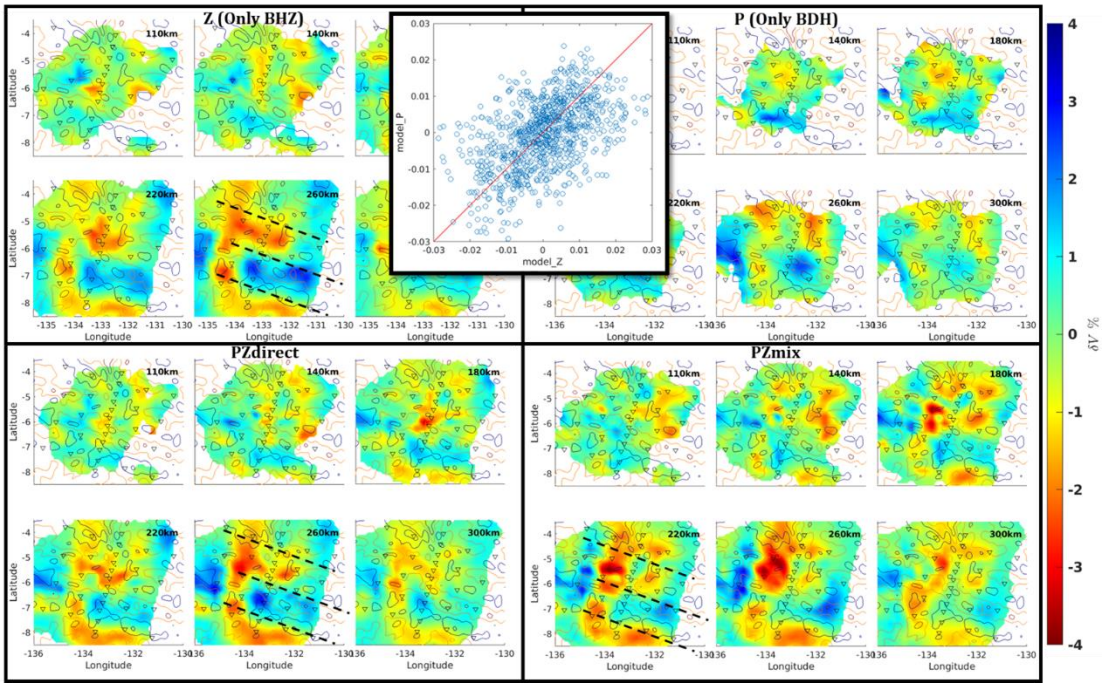

Figure 15. Horizontal slices at depths from 110km to 300km of 3D tomographic velocity perturbation models for 4 data sets, the depth is labeled in the top-right corner of each subplot. Background contour shows the free-air gravity distribution. Parallel dashed lines are used to outline the potential velocity anomaly bands. The top-middle scattering plot shows the comparison between 2 single-channel model values at nodes with 'hit quality' > 0.3, the red line is a 1:1 line.

To further reveal the relationship between mantle velocity variation and topography/gravity variation, I conducted a 2D inversion by enforcing flattening (i.e., no model variation) along a selected horizontal direction. We tested all possible strike directions of the 2D model flattening, seeking the direction that provided the greatest data misfit reduction (Fig. 16(a)). We found that the model that was uniform perpendicular to 15˚ (i.e. features forced to elongate in the 105˚-295˚ direction) produced minimum data misfit and infer that this direction reflects the dominant structural elongation. Interestingly, this direction is roughly orthogonal to the local gravity lineations. It is also close to the APM direction (DeMets et al., 2010). Fig. 17 shows the model cross sections from the 3D and 2D tomographic inversions, respectively.

The prominent features seen in both models are the alternating polarity velocity

anomalies between 200-300km depth with the lateral wavelength of ~300km. We also calculate the average velocity deviation in the model between 200-300km depth as a function of distance along the cross section. This value clearly correlates with the topography/gravity variation along the model profile. The small horizontal offset between velocity/topography variation and gravity variation could be a consequence of lateral resolution issues, or due to a physical offset between bathymetry and deep velocity/thermal/density variations that combine to determine the gravity signal.

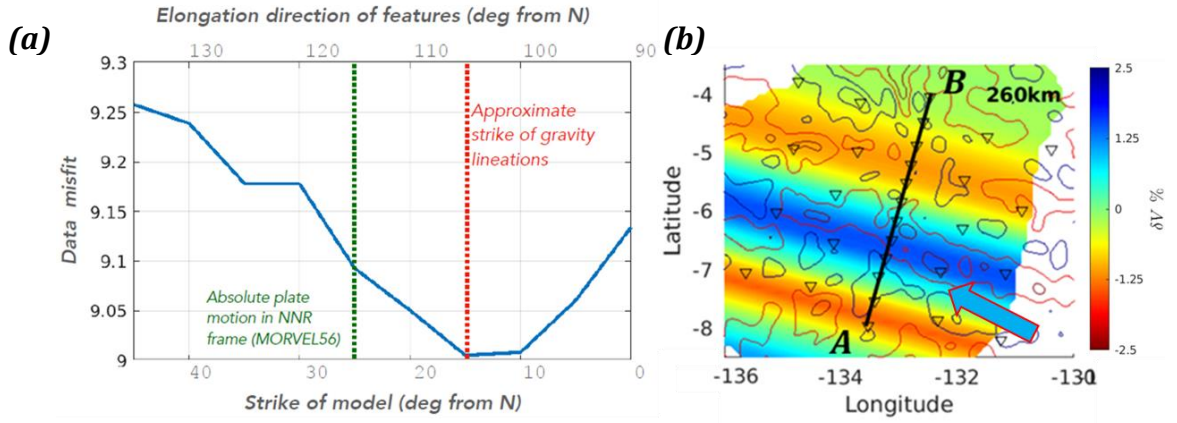

Figure 16. Geometry of vertical 2D model. (1) The relationship between data misfit and the strike direction of the 2D model (2) The velocity map at 260km depth in 2D inversion along 15° profile using 'direct combination' datasets. Line AB shows the profile along which the 2D vertical model was set. The arrow denotes NNR plate motion direction (MORVEL56, DeMets et al. (2010)).

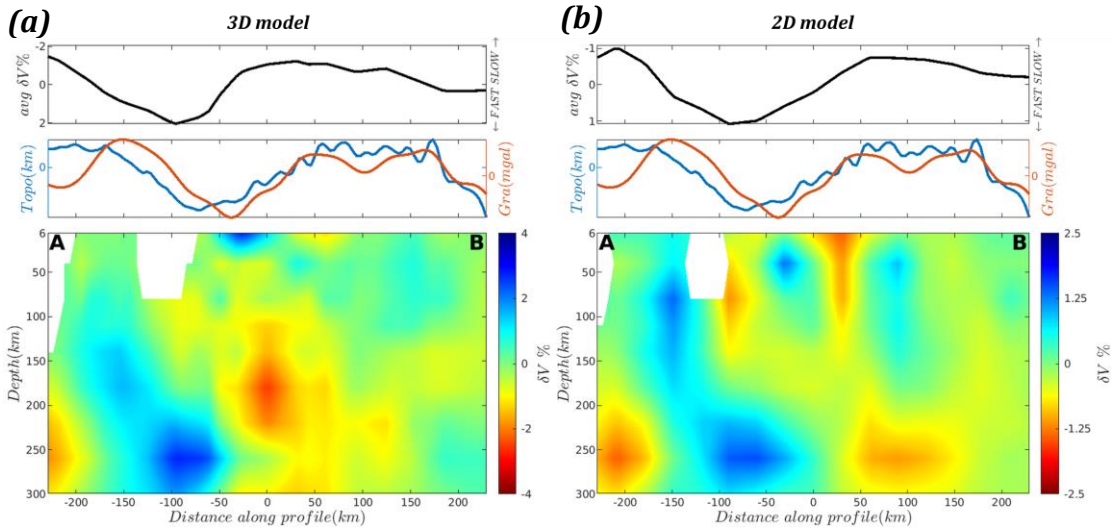

Figure 17. Vertical velocity maps along AB in Fig. 16(b) from 3D and 2D tomographic inversion for 'direct combination' dataset. The black line on the top of each subplot shows the variation of averaged velocity between 200-300km depth. The original topography and gravity maps were both filtered to $2.5 - 5°$.

3. Resolution test and depth constraint

The resolution and reliability of our tomographic inversion result can be evaluated through checkerboard tests (Zelt, 1998). Fig. 18 shows a synthetic test for this research, in the synthetic model regularly flipped velocity anomaly bands parallel with gravity lineations were set at 80-110km as well as 220-260km, and the wavelength of lateral velocity variation was roughly comparable to SSC prediction. After adding gaussian noise with the standard deviation determined during MCCC process, the synthetic data were inverted through our tomographic algorithm to recover the synthetic model. The result indicates that our data do have the coverage to recover the geometry and position of these types of anomalies, but that the amplitudes – especially at the model edges – are poorly recovered due to sparse seismic ray coverage.

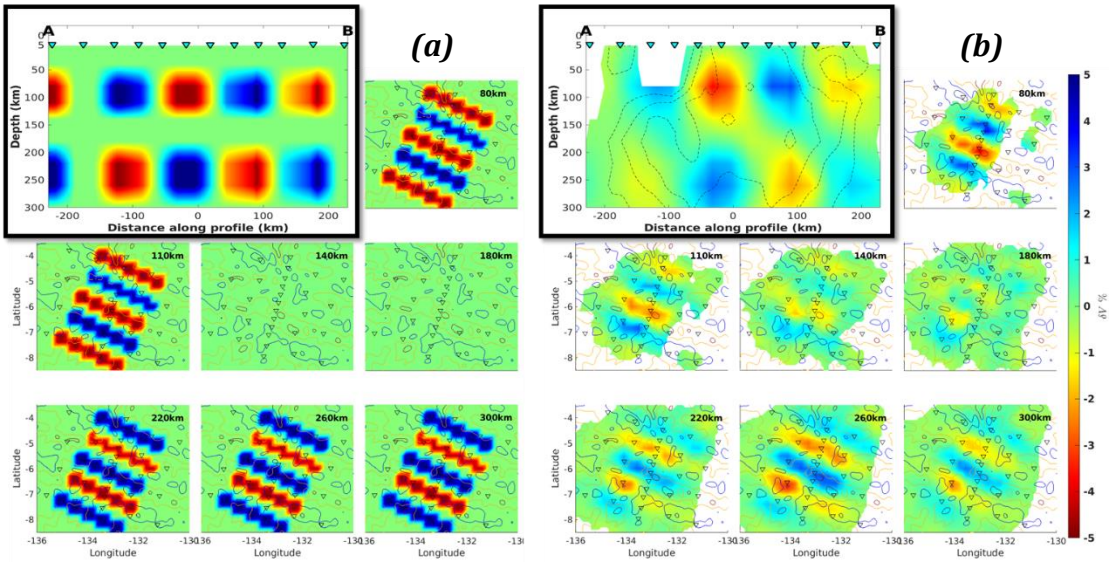

Figure 18. Checkerboard test for OBS array used in this research. Within the black box is the vertical velocity map along profile AB in Fig. 16(b). (a) The input checkerboard model with regularly flipped lateral velocity anomaly bands parallel to gravity anomalies, the anomalies were set at 80-110km and 220-260km with opposite polarities (b) The output tomographic model using 'direct combination' datasets and the optimal regularization determined in Section 3.3.2.

A crucial step to make precise interpretation of the features is to constrain the depth range of the major mantle velocity anomalies, which will give us a window into the asthenospheric parameters (depth and thickness of low-viscosity area etc.) and help to distinguish hypotheses for the non-plume volcanism formation, thus the squeezing test was applied in our research. We tested this using a suite of inversions for which the model nodes below deeper squeezing depth Z_d or above shallower squeezing depth Z_s, were very heavily damped. This damping "squeezes" any structure out of these volumes of the model, and thus forces the inversion to attempt to fit observed data with only a subset of the model and fixed event/station static time (which is identical to that derived from the non-squeezed inversion). By evaluating the fractional reduction in overall data fit for each case, we can thus determine the depths at which the data require velocity anomalies. To quantitatively compare the squeezed models, the weighted variance reduction wvr and the L1 norm of m_2 were calculated for each inversion,

where m_2 is the model obtained through a second iteration of the inversion where squeezing is relaxed to allow the entire model space to try to fit the data residual from the 'squeezed' inversion. If a squeezed model can fit the observed data well, then it will have higher wvr and lower m_2 norm.

Based on the goodness of the squeezed model calculated above, we tried to quantitatively determine the optimal depth range for the prominent mantle velocity anomalies through scanning from the top to the bottom of the model with a depth window containing a certain number of continuous layers. Fig. 19 shows the result for such scan with a 3-layer window. It can be derived from Fig. 19(a) that the optimal 3-layer squeezed model is between 180km and 260km depth, demonstrating that the major mantle velocity anomalies are located at relatively deeper area in our tomographic model. Besides, in the optimal 3-layer model it's clear to see the alternating flipped velocity anomaly bands parallel to local gravity lineations between 220km and 260km depth with the lateral wavelength of ~300km.

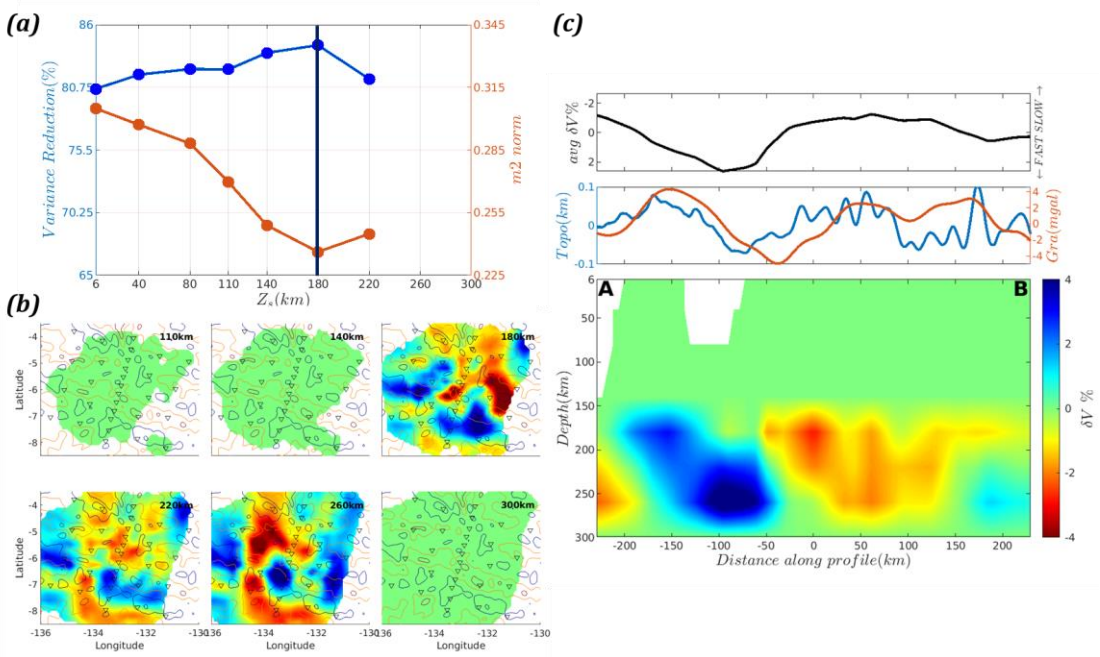

Figure 19. The results for depth scan with a 3-layer window. (a) The goodness of 3-layer squeezed models, the horizontal axis shows the shallower squeezing depth Z_s, the tick

labels denote the vertical spacing of the tomographic model so that each of them corresponds to a tomographic layer, $Z_s = 180km$ actually represents the squeezed model between 180km and 260km depth. The black line shows the numerically optimal depth range (180-260km for this case). (b) The depth slices of the optimal squeezed tomographic model. (c) The vertical slice of the optimal squeezed tomographic model along profile AB in Fig. 16(b).

IV. Discussion

In section III.B.2, we discussed the nature of 5.5-6s negative phase in the RF waveform. To be specific, there could be two potential main sources of this phase during the deconvolution process: (1) a negative phase between 5.5-6s in radial record, which is supposed to originate from NVG features between 50-60km depth (2) the positive water reverberation phase between 5.5-6s in vertical record. To figure out this issue, we tried to obtain an 'average' RF waveform which can reflect regional 1D characteristics in youngORCA deployment region. The 'average' RF was calculated through doing deconvolution with the stacked vertical and radial trace for all events as well as stations passing quality control. Note that before stacking each individual trace was corrected with the polarity by removing the radiation pattern effect, and the stacking was implemented through aligning data points with maximum amplitude within a specific *P*-wave arrival time window. Fig. 20 shows the stacked vertical/radial trace and the 'average' RF, there is a clear minimum (negative phase) between 5.5-6s in the stacked radial waveform and slightly lagging peak in the stacked vertical waveform, indicating that the negative phase between 5.5-6s could be a combination effect of both sources above. More robust judgement can only be made after looking into oldORCA datasets.

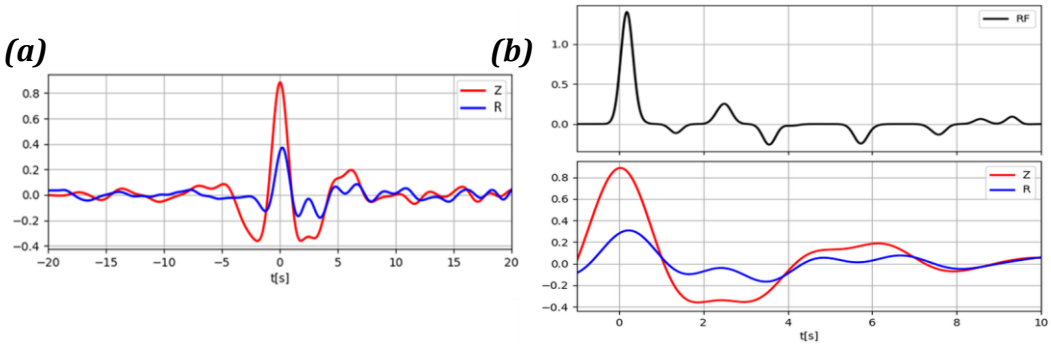

Figure 20. Stacked vertical/radial trace and the 'average' RF within the frequency band 0.1-0.5Hz, there are totally 654 individual traces involved in the stacking for both channels. (a) Stacked trace in a broad time window (b) The top subplot is the 'average' RF calculated from stacked traces, the bottom subplot shows stacked traces in the RF time window for reference.

According to tomographic results, we infer the presence of alternating hot and cold convective cells within the oceanic asthenosphere associated with slow and fast δV_p features. The horizontal lengthscale of the apparent convective cells is ~250 km. These observations provide the first evidence for small-lengthscale differential dynamic support for the oceanic plates. The association of the slow and presumably hot, low-density features with the gravity high points indicates that gravity here is primarily sensitive to dynamically supported short-wavelength topographic extrema, rather than mantle density variations. This in turn implies relatively low elastic strength for the oceanic plate (in the limit that plate rigidity were infinite, free air gravity would respond only to mantle density anomalies).

The amplitude of the observed velocity anomalies is surprisingly high: peak-to-peak dVp values of ±2.5%. For a pyrolytic mantle and assuming purely anharmonic velocity variations with temperature, this would imply ~600˚C lateral temperature variations (Abers and Hacker, 2016). However, assuming anelastic effects are also important, and 1mm grainsize (Behn et al., 2009), the required dT may be as little as ~250˚C. If *in situ* partial melt is present within the upwelling cells due to adiabatic depressurisation, this would further reduce the implied temperature contrast. On the other hand, we note that synthetic tests indicate as much as 2% amplitude loss in the inversion process, which would mean the above temperature gradients are in fact lower bounds.

Assuming a coefficient of thermal expansion of $3x10^{-5}$, and a background asthenospheric density of 3250 kg/m^3, the above temperature estimates translate to 60-25 kg/m^3 lateral density variation.

V. Conclusion

From the CCP profile we observed laterally continuous NVG at ~50-60km depth, this NVG is shallower than the ~85km predicted thermal LAB depth (to 1300˚C isotherm), assuming conductive cooling. But we still need the data from oldORCA deployment to unravel the role played by water phase and NVG features.

From tomographic result we observed alternate velocity anomaly bands parallel to local gravity lineations at ~180-260km depth, the P-wave velocity variation correlates well with the topography/gravity variation along the direction orthogonal to gravity lineations, which seems to support SSC theory.

References

Abers, G. A., and Hacker, B. R., 2016, A MATLAB toolbox and Excel workbook for calculating the densities, seismic wave speeds, and major element composition of minerals and rocks at pressure and temperature: Geochemistry, Geophysics, Geosystems, v. 17, no. 2, p. 616-624, https://doi.org/10.1002/2015gc006171.

Aki, K., Christoffersson, A., and Husebye, E. S., 1977, Determination of the three-dimensional seismic structure of the lithosphere: Journal of Geophysical Research (1896-1977), v. 82, no. 2, p. 277-296, https://doi.org/10.1029/JB082i002p00277.

Ballmer, M. D., Conrad, C. P., Smith, E. I., and Harmon, N., 2013, Non-hotspot volcano chains produced by migration of shear-driven upwelling toward the East Pacific Rise: Geology, v. 41, no. 4, p. 479-482, https://doi.org/10.1130/g33804.1.

Ballmer, M. D., van Hunen, J., Ito, G., Bianco, T. A., and Tackley, P. J., 2009, Intraplate volcanism with complex age-distance patterns: A case for small-scale sublithospheric convection: Geochemistry, Geophysics, Geosystems, v. 10, no. 6, p. n/a-n/a, https://doi.org/10.1029/2009gc002386.

Ballmer, M. D., van Hunen, J., Ito, G., Tackley, P. J., and Bianco, T. A., 2007, Non-hotspot volcano chains originating from small-scale sublithospheric convection: Geophysical Research Letters, v. 34, no. 23, p. n/a-n/a, https://doi.org/10.1029/2007gl031636.

Behn, M., Hirth, G., and Elsenbeck, J., 2009, Implications of grain size evolution on the seismic structure of the oceanic upper mantle: Earth and Planetary Science Letters, v. 282, p. 178-189, https://doi.org/10.1016/j.epsl.2009.03.014.

Buck, W. R., 1985, When does small-scale convection begin beneath oceanic lithosphere?: Nature, v. 313, no. 6005, p. 775-777, https://doi.org/10.1038/313775a0.

Crawford, W. C., and Webb, S. C., 2000, Identifying and Removing Tilt Noise from Low-Frequency (<0.1 Hz) Seafloor Vertical Seismic Data: The Bulletin of the Seismological Society of America, v. 90, p. 952-963.

Crosby, A. G., McKenzie, D., and Sclater, J. G., 2006, The relationship between depth, age and gravity in the oceans: Geophysical Journal International, v. 166, no. 2, p. 553-573, https://doi.org/10.1111/j.1365-246X.2006.03015.x.

DeMets, C., Gordon, R. G., and Argus, D. F., 2010, Geologically current plate motions: Geophysical Journal International, v. 181, no. 1, p. 1-80, https://doi.org/https://doi.org/10.1111/j.1365-246X.2009.04491.x.

Harmon, N., Forsyth, D. W., and Scheirer, D. S., 2006, Analysis of gravity and topography in the GLIMPSE study region: Isostatic compensation and uplift of the Sojourn and Hotu Matua Ridge systems: Journal of Geophysical Research: Solid Earth, v. 111, no. B11, p. n/a-n/a, https://doi.org/10.1029/2005jb004071.

Harmon, N., Forsyth, D. W., Weeraratne, D. S., Yang, Y., and Webb, S. C., 2011, Mantle heterogeneity and off axis volcanism on young Pacific lithosphere: Earth and Planetary Science Letters, v. 311, no. 3-4, p. 306-315, https://doi.org/10.1016/j.epsl.2011.09.038.

Haxby, W. F., and Weissel, J. K., 1986, Evidence for small-scale mantle convection from Seasat altimeter data: Journal of Geophysical Research: Solid Earth, v. 91, no. B3, p. 3507-3520, https://doi.org/10.1029/JB091iB03p03507.

Hernlund, J. W., Tackley, P. J., and Stevenson, D. J., 2008, Buoyant melting instabilities beneath extending lithosphere: 1. Numerical models: Journal of Geophysical Research, v. 113, no. B4, https://doi.org/10.1029/2006jb004862.

Kennett, B. L. N., 1981, Elastic Wave Propagation in Stratified Media, *in* Yih, C.-S., ed., Advances in Applied Mechanics, Volume 21, Elsevier, p. 79-167.

Ligorría, J. P., and Ammon, C. J., 1999, Iterative deconvolution and receiver-function estimation: Bulletin of the Seismological Society of America, v. 89, no. 5, p. 1395-1400.

McNamara, D. E., Hutt, C. R., Gee, L. S., Benz, H. M., and Buland, R. P., 2009, A Method to Establish Seismic Noise Baselines for Automated Station Assessment: Seismological Research Letters, v. 80, no. 4, p. 628-637, https://doi.org/10.1785/gssrl.80.4.628.

Morgan, W. J., Shagam, R., Hargraves, R. B., Morgan, W. J., Van Houten, F. B., Burk, C. A., Holland, H. D., and Hollister, L. C., 1972, Plate Motions and Deep Mantle Convection, Studies in Earth and Space Sciences, Volume 132, Geological Society of America, p. 0.

Olugboji, T. M., Park, J., Karato, S.-i., and Shinohara, M., 2016, Nature of the seismic lithosphere-asthenosphere boundary within normal oceanic mantle from high-resolution receiver functions: Geochemistry, Geophysics, Geosystems, v. 17, no. 4, p. 1265-1282, https://doi.org/10.1002/2015gc006214.

Parsons, B., and McKenzie, D., 1978, Mantle convection and the thermal structure of the plates: Journal of Geophysical Research: Solid Earth, v. 83, no. B9, p. 4485-4496, https://doi.org/10.1029/JB083iB09p04485.

Parsons, B., and Sclater, J. G., 1977, An analysis of the variation of ocean floor bathymetry and heat flow with age: Journal of Geophysical Research (1896-1977), v. 82, no. 5, p. 803-827, https://doi.org/10.1029/JB082i005p00803.

Richter, F. M., and Parsons, B., 1975, On the interaction of two scales of convection in the mantle: Journal of Geophysical Research, v. 80, no. 17, p. 2529-2541, https://doi.org/10.1029/JB080i017p02529.

Russell, J. B., Eilon, Z., and Mosher, S. G., 2019, OBSrange: A New Tool for the Precise Remote Location of Ocean‐Bottom Seismometers: Seismological Research Letters, https://doi.org/10.1785/0220180336.

Sandwell, D. T., Winterer, E. L., Mammerickx, J., Duncan, R. A., Lynch, M. A., Levitt, D. A., and Johnson, C. L., 1995, Evidence for diffuse extension of the Pacific Plate from Pukapuka ridges and cross-grain gravity lineations: Journal of Geophysical Research: Solid Earth, v. 100, no. B8, p. 15087-15099, https://doi.org/10.1029/95jb00156.

Schmandt, B., and Humphreys, E., 2010, Seismic heterogeneity and small-scale convection in the southern California upper mantle: Geochemistry, Geophysics, Geosystems, v. 11, no. 5, p. n/a-n/a, https://doi.org/10.1029/2010gc003042.

Stachnik, J. C., Sheehan, A. F., Zietlow, D. W., Yang, Z., Collins, J., and Ferris, A., 2012, Determination of New Zealand Ocean Bottom Seismometer Orientation via Rayleigh-Wave Polarization: Seismological Research Letters, v. 83, no. 4, p. 704-713, https://doi.org/10.1785/0220110128.

Stein, C. A., and Stein, S., 1992, A model for the global variation in oceanic depth and heat flow with lithospheric age: Nature, v. 359, no. 6391, p. 123-129, https://doi.org/10.1038/359123a0.

Turcotte, D., and Schubert, G., 2014, Geodynamics, Cambridge, Cambridge University Press.

VanDecar, J. C., and Crosson, R. S., 1990, Determination of teleseismic relative phase arrival times using multi-channel cross-correlation and least squares: Bulletin of the Seismological Society of America, v. 80, no. 1, p. 150-169.

Weeraratne, D. S., Forsyth, D. W., Yang, Y., and Webb, S. C., 2007, Rayleigh wave tomography beneath intraplate volcanic ridges in the South Pacific: Journal of Geophysical Research, v. 112, no. B6, https://doi.org/10.1029/2006jb004403.

Zelt, C. A., 1998, Lateral velocity resolution from three-dimensional seismic refraction data: Geophysical Journal International, v. 135, p. 1101.

Zhu, L., 2000, Crustal structure across the San Andreas Fault, southern California from teleseismic converted waves: Earth and Planetary Science Letters, v. 179, no. 1, p. 183-190, https://doi.org/https://doi.org/10.1016/S0012-821X(00)00101-1.